communications earth & environment

Article

https://doi.org/10.1038/s43247-024-01452-1

Magma titanium and iron contents dictate crystallization timescales and rheological behaviour in basaltic volcanic systems

Check for updates

Fabrizio Di Fiore [1] ✉, Alessandro Vona [2], Danilo Di Genova [3], Alessio Pontesilli [1], Laura Calabrò [4], Silvio Mollo[1,5], Jacopo Taddeucci [1], Claudia Romano[2] & Piergiorgio Scarlato [1]

Magma ascending through Earth's crust undergoes complex chemical and physical changes that may induce crystallization, a process that contributes to lead the magmatic system toward a thermodynamic state of equilibrium. The diverse cooling and deformative regimes suffered by magmas heavily influence crystallization rates, solidification timescales, and consequently, the rheological evolution of magma. This, in turn, significantly impacts the dynamics of volcanic plumbing systems and the associated eruptive styles. Here, we investigate the rheological changes in Stromboli magma (Italy) during disequilibrium crystallization under non-isothermal *subliquidus* conditions. By systematically varying the cooling rate (1-10 °C/min) and the shear rate (1-10 s^{-1}), we find that cooling rates significantly influence the solidification path of the basalt, whereas shear rates have a subordinate effect. By comparing our results with literature data on basalts from Mt. Etna (Italy), characterized by higher TiO_2 and FeO_{tot} contents, we observed distinct timescales and rates of solidification, contributing to unique eruptive dynamics in these volcanic plumbing systems.

Basaltic volcanism is the dominant volcanic activity on rocky planets within the solar system[1–3]. Basaltic eruptions typically manifest as both mildly explosive lava fountaining and effusive lava flow[4–8]. Although less frequent in active volcanoes, highly explosive sub-Plinian and Plinian basaltic eruptions (e.g.[9–14]) are more hazardous events with potentially larger impact on human activities and infrastructure.

It is well established that the eruptive style is primarily governed by the rate of decompression and the effectiveness of gas-phase separation from the magma[15–19]. The latter is influenced by the magma viscosity, which governs the decoupling between the liquid-crystals suspension and the exsolving gas phases[5,20–22].

Over the past decade, extensive efforts have been devoted to experimentally studying the rheological changes of melts feeding eruptions under disequilibrium conditions, with a specific focus on basaltic compositions. Basalts are characterized by low silica content (i.e., 48–52 wt.% of SiO_2) and relatively low viscosity[23–28], which make these melts prone to rapid syn-eruptive crystallization that significantly impacts magma viscosity, which in turn controls the eruptive style[6,7,24,25,28–33]. Basaltic magmas undergo a range of cooling and deformation rates that may simultaneously promote or hinder crystallization[24,27,28,34–39]. Generally, due to the extent of disequilibrium conditions and low viscosity, rapid crystallization kinetics prevail[32,40–43].

To parameterize the rheological evolution of basaltic melts in response to systematic variations in both cooling and shear rates, we carried out a set of Cooling Deformation Experiments (CDE) on a Stromboli high-K basalt (Italy). The comparison of our findings with published disequilibrium rheology data for Mt. Etna trachybasalt (Italy) reveals a divergent rheological evolution of these two compositional systems, showing different timescales of crystallization resulting from a more pronounced impact of the cooling rate on the rheological evolution of melt from Stromboli with respect to those from Mt. Etna. Ultimately, implications from this comparison are discussed and extended to natural eruptive scenarios.

Results

Stromboli pure liquid viscosity

Table 1 lists the η_{liquid} values derived from Concentric Cylinder (CC) measurements and Differential Scanning Calorimetry (DSC).

[1]Istituto Nazionale di Geofisica e Vulcanologia, Sezione di Roma 1, Via di Vigna Murata 605, 00143 Roma, Italy. [2]Dipartimento di Scienze, Università degli Studi Roma Tre, L.go San Leonardo Murialdo 1, 00146 Roma, Italy. [3]Institute of Science, Technology and Sustainability for Ceramics (ISSMC), National Research Council (CNR), Via Granarolo 64, Faenza 48018, Italy. [4]Istituto Nazionale di Geofisica e Vulcanologia, Sezione di Pisa, Via Cesare Battisti, 53, 56125 Pisa, Italy. [5]Dipartimento di Scienze della Terra, Sapienza-Università di Roma, P.le Aldo Moro 5, 00185 Roma, Italy. ✉e-mail: fabrizio.difiore@ingv.it

Table 1 | Viscosity data of anhydrous Stromboli melt from concentric cylinder (CC) and differential scanning calorimetry (DSC) measurements

Technique	T (°C)	T (K)	η_a Log (Pa s)
CC	1400	1673.15	0.68
CC	1350	1623.15	0.93
CC	1325	1598.15	1.05
CC	1300	1573.15	1.18
CC	1275	1548.15	1.32
CC	1250	1523.15	1.47
DSC	657.2	930.35	11.98
DSC	662.5	935.65	11.67
DSC	690	963.15	10.56
DSC	697	970.15	10.24
Viscosity models fitting parameters			
	A	**B**	**C**
VFT	−4.68	5829.2	579.9
[a]GRD	−4.55	5586.1	596.4
	A	**Tg (in K)**	**m**
[b]ANN	−2.9	932.08	42.22

VFT, GRD and ANN equation parameters obtained by data fitting are also reported.
[a]GRD from Giordano et al.[23]
[b]ANN from Langhammer et al.[44]

The η_{liquid} values measured by CC at high-T ranges from $10^{0.68}$ to $10^{1.47}$ Pa s within the temperature interval between 1400–1250 °C (Table 1). The estimated η_{liquid} by DSC analysis varies from $10^{10.24}$ to $10^{11.98}$ Pa s over a temperature interval between 697-657 °C (Table 1).

The η_{liquid} values obtained from both high-temperature and low-temperature measurements were fitted via the Vogel-Fulcher-Tammann (VFT) equation:

$$Log\eta_{liquid} = A + \frac{B}{(T - C)} \quad (1)$$

where $A = -4.68$, $B = 5829.2$, and $C = 579.9$ are the fitting parameters and T is the temperature in Kelvin. Equation (1) reproduces data with a Root Mean Squared Relative Error (RMSRE) of ±0.025 Log units (Supplementary Fig. 1).

Data match the prediction of both the Giordano–Dingwell–Russell (GRD) model[23] with a RMSRE of ±0.12 Log units and the Artificial Neural Network (ANN) model[44] with a RMSRE of ±0.12 Log units.

Apparent and normalized viscosity from Cooling Deformation Experiments

Figure 1a, b display the evolutions of apparent viscosity (η_a) with respect to temperature (T) and time (t), respectively, under different cooling rates (q) and shear rates ($\dot{\gamma}$) (Supplementary Fig. 2). In all CDE experiments at *superliquidus* conditions, the rheological evolution of the melt follows the VFT model prediction, ruling out significant thermal lag during measurements. Viscosity consistently increases as temperature decreases until the η_a–T curve departs from the modeled pure liquid viscosity. This departure signifies the onset of crystallization and is observed in all experiments except for the run carried out at q of 10 °C/min, which shows no deviation from the η_{liquid} curve within the temperature range between 1400 and 1022 °C. At q of 1, 3 and 5 °C/min, the temperature at which the rheological departure from η_{liquid} is observed (i.e., onset of crystallization; T_{onset}; see Supplementary Table 1) shifts from 1149 to 1049 °C as q increases from 1 to 5 °C/min and $\dot{\gamma}$ decreases from 10 to 1 s^{-1} (Fig. 1a and Table 2). The time required to observe the onset of crystallization (t_{onset}) decreases from 283 min to 64 min as both q and $\dot{\gamma}$ increase (Fig. 1b and Table 2). The experiments were manually halted as the shear stress threshold was approached. Final temperatures (T_{final}) range from 1137 to 1010 °C, with increasing q and decreasing $\dot{\gamma}$ (Fig. 1a), and the overall experimental time duration (t_{final}) decreases from 302 to 68 min with increasing both q and $\dot{\gamma}$ (Fig. 1b).

Figure 1c, d illustrate the impact of crystallization on the normalized viscosity (η_x) with respect to T and t, respectively. The final η_x values range from $10^{0.50}$ (for $q = 5$ °C/min and $\dot{\gamma} = 10\ s^{-1}$) to $10^{1.79}$ (for $q = 1$ °C/min and $\dot{\gamma} = 1\ s^{-1}$, Table 2).

Discussion

Thermo-rheological diagram for Stromboli basalt

Integrating data from Cooling Deformation Experiments (CDE) of this study with near-equilibrium crystallization viscosity data (Isothermal Deformation Experiments–IDE) from literature[24] allows us to define and quantify the viscosity-temperature (η-T) space in which the crystallization affects the rheological evolution of the anhydrous Stromboli high-K basalt under air redox conditions.

As depicted in Fig. 2, at *superliquidus* temperatures, the melt's viscosity aligns with the pure liquid viscosity derived from Eq. (1) until it crosses the *liquidus* temperature ($T_{liquidus}$). The lower-η and the upper-η boundaries diverge from the *liquidus* symbol, providing a semiquantitative representation of the η-T space for the two-phase (melt+crystals) rheology of the Stromboli high-K basalt. At *subliquidus* temperatures, the lower-η boundary corresponds to the minimum viscosity values attainable by a melt subjected to a cooling rate (q) higher than its critical q (supercooled melt[28,39,45,46]). This boundary is represented by the trend derived from Eq. (1), which models the pure liquid viscosity also at *subliquidus* temperatures. On the other hand, the upper-η boundary qualitatively defines the highest viscosity achievable by the basaltic magma at *subliquidus* temperatures. These viscosity values are related to a time-independent, near-equilibrium crystallization of the melt, indicating the highest possible crystal content attainable at any temperature considered. These viscosity values are derived from a set of IDE carried out on a Stromboli basalt within a temperature range between 1187 and 1157 °C, under a fixed shear rate ($\dot{\gamma}$) of 4.26 s^{-1} and under air redox conditions[24].

The η-T window delineated by lower-η and upper-η boundaries encompasses all possible combinations of η-T values associated with melt disequilibrium conditions. Our CDE were conducted within this window of disequilibrium crystallization (Fig. 2). Consistent with previous studies on mafic melts[25,27,28,39,45,47], viscosity data from CDE reveal the contrasting impacts of cooling rate q and $\dot{\gamma}$ on the rheological evolution of the melt. Specifically, the onset of crystallization and the subsequent viscosity departure progressively shifts at lower T and higher η as the value of q increases (Fig. 2).

This is due to the balance effect between the kinetics of crystallization and q. In detail, higher q applied leads to faster viscosity increase of the melt through time, lowering the diffusion of cations in the melt phase. Consequently, the crystal nucleation is hampered and shifted at lower T with increasing q until a critical q is applied[28,37,39,46]. In the latter case, the crystallization is kinetically suppressed, resulting in the formation of only glass phase. Conversely, when comparing measurements with the same q, an increase in $\dot{\gamma}$ leads to the onset of crystallization occurring at higher temperatures (i.e., the curves shift toward the upper-η boundary Fig. 2). With increasing stirring the mobility of cations through the melt is enhanced, thus favoring their random collisions and, hence, the crystal nucleation and growth processes[34,48–50]. As a result, an increase of $\dot{\gamma}$ promotes at higher T the onset of crystallization.

While the thermo-rheological diagram presented in Fig. 2 is a valuable tool for visualizing the η-T window of the Stromboli basaltic melt, it does not capture the influence of q and $\dot{\gamma}$ applied during experiments on the timescales of crystallization. Particularly, the timescales of crystallization are a crucial aspect of the rheological evolution of the melt under strong disequilibrium conditions[28,32,33,50], reflecting the transient viscosity observed during measurements. One of the advantages of the CDE technique is its capability to monitor in real-time the viscosity changes resulting from the combined effects of q and $\dot{\gamma}$. To enhance the visualization of crystallization timescales for different cooling paths, these latter are presented in a Time-Temperature-Transformation (*TTT*) diagram (Fig. 3).

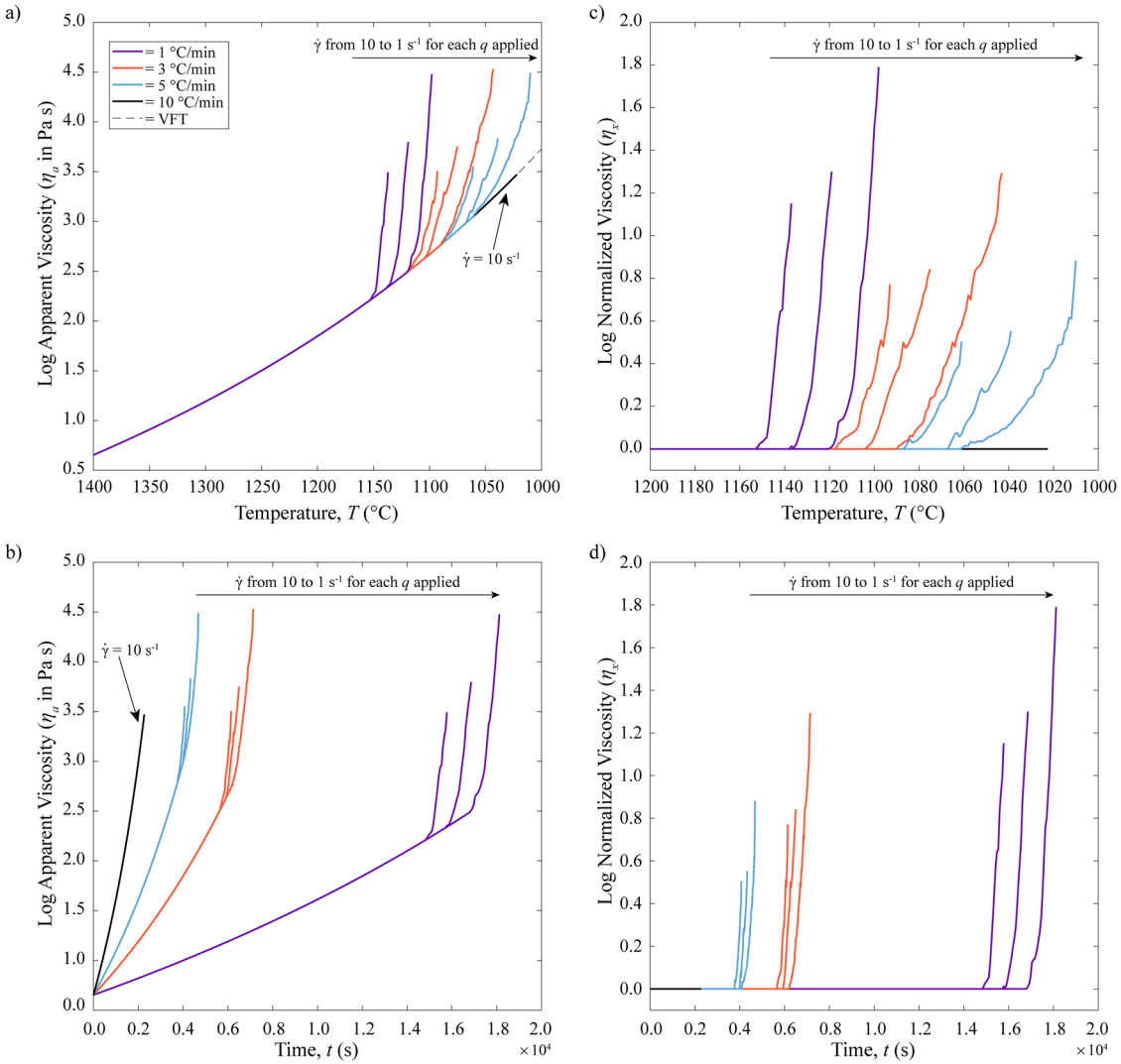

Fig. 1 | Summary of the Cooling Deformation Experiments (CDE) carried out on Stromboli high-K basalt. (a and b) Changes in apparent viscosity (η_a) as a function of temperature (**a**) and time (**b**). The dashed line in **a** represents the modeling of melt viscosity derived from Eq. (1). **c**, **d** Changes in normalized viscosity (η_x) as a function of temperature (**c**) and time (**d**). Note the lack of crystallization onset for the range of T investigated in the experiment carried out at q of 10 °C/min and $\dot{\gamma}$ of 10 s^{-1}.

Figure 3 displays the temperatures and times corresponding to the crystallization onset and experiment interruption. Across the studied range of q and $\dot{\gamma}$, variations in T-t related to the onset of crystallization are more closely tied to the changes in q than in $\dot{\gamma}$. This observation suggests that q plays a pivotal role in controlling the onset of crystallization in Stromboli basalt for both T_{onset} and t_{onset} (Table 2). This observation aligns with recent studies describing similar behavior in various mafic compositions[25,27,28,39,47]. In these studies, the crystallization takes place at progressively lower T and shorter t with increasing q until it is completely suppressed within the experimental ranges investigated. Among our experiments, the cooling rate at which no crystallization is observed during a CDE measurement is 10 °C/min. Consequently, the critical cooling rate (i.e., the threshold above which the crystallization is suppressed) falls between 5 and 10 °C/min. Referring to the investigated range of T and t, this value is consistent with prior investigation of melts characterized by low viscosities and rapid crystallization kinetics[28,39,45,46]. Conversely, the effect of $\dot{\gamma}$ is evident in anticipating at higher T and shorter t the onset of crystallization. By comparing the crystallization onsets it can be observed from Fig. 3 that they occur at progressively higher T and shorter t with increasing deformation rate from 1 to 10 s^{-1} for each applied q.

Table 2 | Results of disequilibrium viscosity measurements from CDE

q (°C/min)	$\dot{\gamma}$ (s^{-1})	T_{onset} (°C)	t_{onset} (min)	T_{final} (°C)	t_{final} (min)	η_a Log (Pa s)	η_x Log (units)
1	1	1117	283	1098	302	4.48	1.79
1	5	1133	267	1119	281	3.80	1.30
1	10	1149	251	1137	263	3.49	1.15
3	1	1084	105	1043	119	4.53	1.29
3	5	1100	100	1075	108	3.75	0.84
3	10	1113	96	1093	102	3.50	0.77
5	1	1049	70	1010	78	4.49	0.88
5	5	1065	67	1039	72	3.83	0.55
5	10	1080	64	1061	68	3.55	0.50
10	10	-	-	1022	38	3.47	0.00

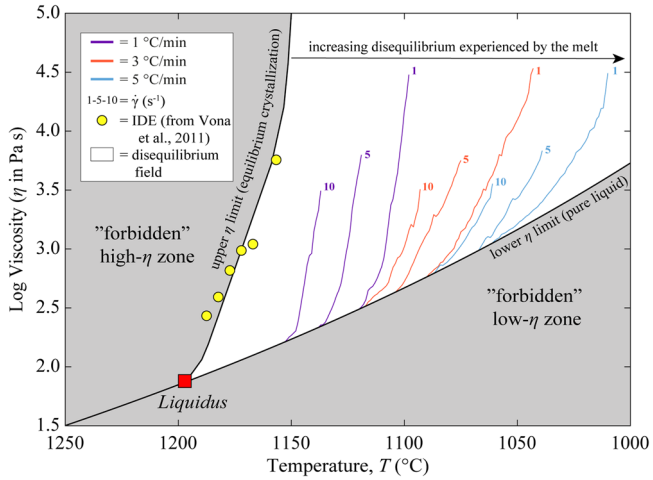

Fig. 2 | Viscosity-temperature regime diagram for the Stromboli high-K basalt at atmospheric pressure (i.e., $P = 1$ atm) and air fO_2 conditions (i.e., log $fO_2 = -0.68$). The lower limit is defined by the pure liquid viscosity derived from Eq. (1). The upper boundary departs from a *liquidus T* of 1195 °C estimated through MELTS, and it is qualitatively outlined from literature data[24]. In the viscosity-temperature space depicted by these two boundaries the rheological evolution paths under disequilibrium conditions for the Stromboli magma takes place (see text for more details).

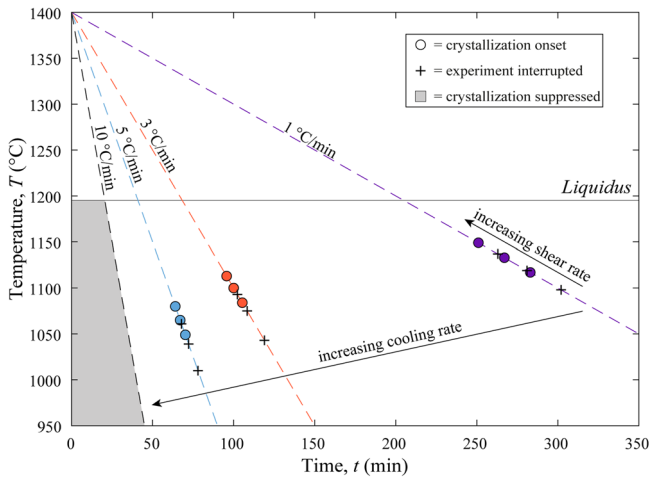

Fig. 3 | Time-temperature-transformation (*TTT*) diagram of the Stromboli high-K basalt. The diagram illustrates the impact of q and $\dot{\gamma}$ on timescales of crystallization. Crystallization onset (circles) and interruption of the experiment (cross) are plotted as t_{onset}–T_{onset} and t_{end}–T_{end} pairs, respectively. Dashed lines represent cooling rates of 1 °C/min (purple), 3 °C/min (orange), 5 °C/min (light blue) and 10 °C/min (black). Note that the symbols are larger than the t–T uncertainties.

To parameterize the influence of q and $\dot{\gamma}$ on the crystallization onset, the T_{onset} values from CDE (Table 3) were fitted adopting a bilinear function (Fig. 4), following the same approach described in previous study[28]:

$$T_{onset} = a \times q + b \times \dot{\gamma} + c \quad (2)$$

where q is in °C s^{-1}, $\dot{\gamma}$ is in s^{-1}, and the coefficients are $a = -1025.12 \pm 46.21$ s, $b = 3.38 \pm 0.19$ °C s, and $c = 1132.24 \pm 3.02$ °C.

The T_{onset} values are well-reproduced by the Eq. (2) with a coefficient of determination (R^2) of 0.98 and standard error of estimate (SEE) of 14.36.

Table 3 | Chemical compositions of the starting material and CDE post-run re-melted glass

Oxide	Starting Material		CDE post-run	
	wt. %	s.d.	wt. %	s.d.
SiO_2	51.11	0.32	51.18	0.29
TiO_2	0.92	0.05	0.95	0.04
Al_2O_3	15.65	0.19	15.70	0.18
FeO	8.08	0.14	8.03	0.16
MnO	0.18	0.02	0.17	0.02
MgO	7.24	0.12	7.20	0.11
CaO	11.72	0.15	11.64	0.16
Na_2O	2.47	0.06	2.50	0.05
K_2O	2.10	0.03	2.09	0.04
P_2O_5	0.55	0.02	0.54	0.02

Data are reported in wt.% and correspond to the average of 10 analyses.

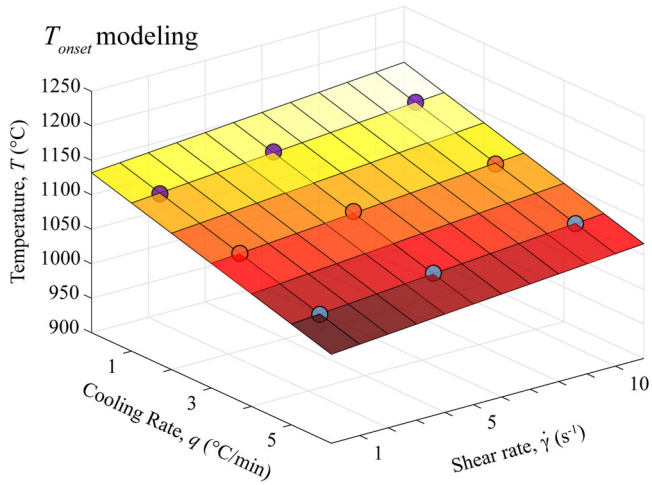

Fig. 4 | Parameterization of crystallization onset temperature of high-K basaltic melt from Stromboli as a function of cooling rate and shear rate. Circle symbols correspond to q of 1 °C/min (purple), 3 °C/min (orange), 5 °C/min (light blue). Error bars are within the symbols.

Based on Eq. (6), the timescales of the onset of crystallization can be also estimated as:

$$t_{onset} = \frac{T_0 - T_{onset}}{q} \quad (3)$$

where T_0 is the *superliquidus T* of CDE.

It is worth noting that this empirical model has been specifically calibrated for the Stromboli high-K basalt within the described range of q and $\dot{\gamma}$ and for the T and t used in the CDE. Therefore, any extrapolations beyond these calibration bounds may introduce a certain degree of uncertainty.

Insights into basaltic systems

To explore and characterize the influence of q and $\dot{\gamma}$ on the high-T disequilibrium rheology of basaltic systems, our rheological dataset is compared and discussed alongside other rheological datasets obtained on trachybasalts erupted at Mt. Etna (Italy). Several reasons underlie this choice:

1) CDE data from Mt. Etna melts are well-represented in the literature[27,28]. Notably, the data presented by Di Fiore et al.[28] mirror the

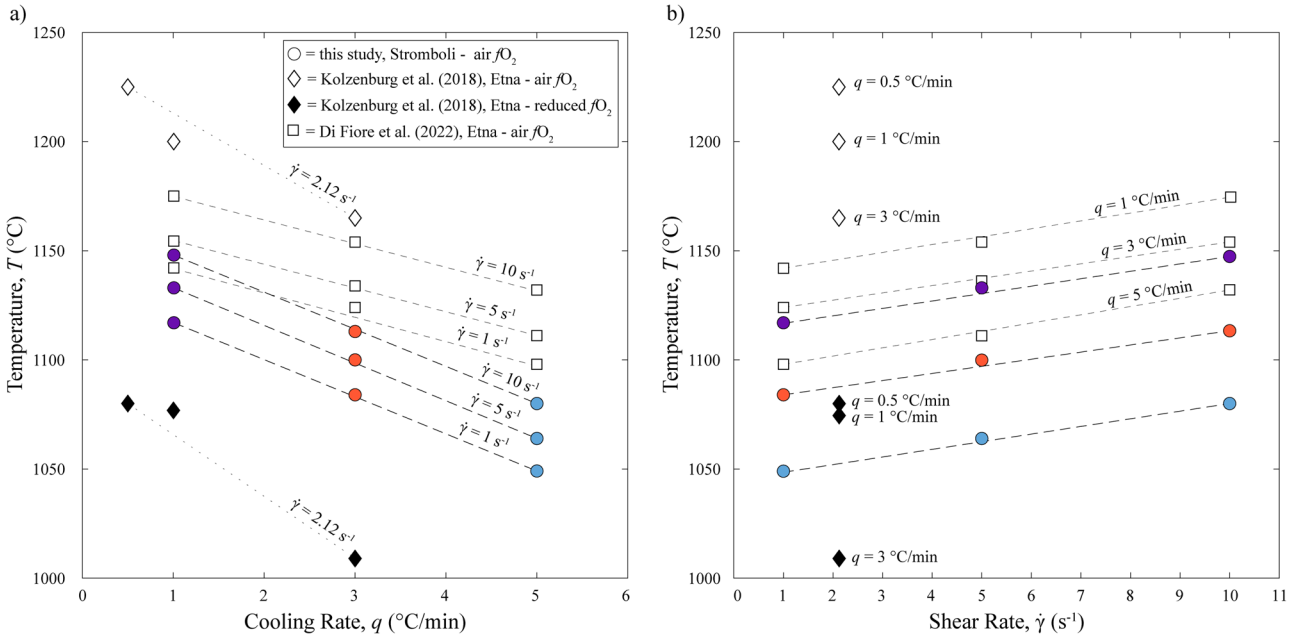

Fig. 5 | Crystallization onset temperature values of Stromboli high-K basalt (this study) and Etna trachybasalts[27,28] under disequilibrium conditions. In **a** the q-T values of the crystallization onset are reported. In **b** $\dot{\gamma}$-T values of the crystallization onset are reported. Colors in the circle symbols (this study) correspond to q of 1 °C/min (purple), 3 °C/min (orange), 5 °C/min (light blue), respectively. The error is within the symbols. Air fO_2 conditions correspond to $\log fO_2 = -0.68$ and reduced fO_2 conditions correspond to $\log fO_2 = -9.15$.

experimental approach employed in this study (i.e., the systematic variations of q and $\dot{\gamma}$), allowing for a direct comparison between these two basaltic systems;

2) recent studies[51–53] have identified a chemical threshold between these two basaltic magmas dictating nanocrystallization and the degassing behavior. These studies have primarily focused on the viscosity at low-T, but a comparative analysis of the crystallization kinetics typically encountered at high-T during magma ascent and eruption at the syn-eruptive stage, to date, is still lacking;

3) despite both being basaltic systems, Stromboli and Mt. Etna exhibit distinct volcanic activities, with their eruptive styles intricately linked to the disequilibrium rheology of the magma[6,32,52].

Crystallization onset

Figure 5 shows the T_{onset} identified for the Stromboli high-K basalt (Supplementary Table 2) and two trachybasalts from Mt. Etna[27,28] obtained through CDE carried out at variable q and $\dot{\gamma}$ (Fig. 5a, b, respectively). Note that all the T_{onset} were recalculated according to the methodology described in the method section and provided in Supplementary Table 2. In Kolzenburg et al.[27], two sets of CDE were carried out under different oxygen fugacity (fO_2) conditions, namely air fO_2 (i.e. $\log fO_2 = -0.68$) and reduced fO_2 ($\log fO_2 = -9.15$) conditions. These experiments commenced at *superliquidus* T of 1300 °C, with q values of 0.5, 1 and 3 °C/min and $\dot{\gamma}$ value of 2.12 s^{-1} for each redox state condition. In Di Fiore et al.[28], both q and $\dot{\gamma}$ are the same as those used in this study, starting from *superliquidus* T of 1400 °C and air fO_2 conditions.

Upon comparing the data from these studies, the overall trend depicted in Fig. 5 reveals that the T_{onset} values decrease with increasing q and decreasing $\dot{\gamma}$. The two trachybasaltic melts from Mt. Etna exhibit significant differences in their T_{onset} values under air fO_2 conditions, despite having similar chemical compositions (Supplementary Table 3) and measured under similar experimental conditions. This discrepancy can be attributed to a different *superliquidus* treatment to which the melt was subjected. In turn, these different treatments affect the nucleation incubation time[54,55] and related timescales. In Kolzenburg et al.[27], the *superliquidus* treatment for CDE carried out under air fO_2 involved stirring the melt at 2.12 s^{-1} for a dwell time of 2–7 h at a T of 1320 °C (note that the reduced fO_2 conditions differ only in the dwell time of 36 h). Conversely, in Di Fiore et al.[28] the pre-experiment melt homogenization entailed stirring the melt at 10 s^{-1} for over 4 h and at a dwell T of 1400 °C.

In the experiments carried out under air fO_2, it is evident that the T_{onset} values for the Stromboli melt are markedly lower than those determined for Mt. Etna melts (Fig. 5). The higher onset temperatures for crystallization observed in Mt. Etna melt under air fO_2 conditions can be attributed to the different mineral phases that saturate the melt during cooling. Although the CDE technique does not permit post-run sampling, the crystallization sequence can be inferred from the mineralogical assemblage described in literature study[24]. This study involved a set of Isothermal Deformation Experiments (IDE) at different dwell temperatures using Stromboli and Mt. Etna melts. The analysis of post-run products of Stromboli melt[24,56] revealed a gradually more pervasive crystallization of plagioclase (from 10.7 to 22.9 vol.%) with decreasing T (from 1187 to 1157 °C). Subordinate crystallization of clinopyroxene (2.7 vol.%) and Fe-Ti oxides (1.6 vol.%) at 1157 °C. In contrast, the post-run product from Mt. Etna exhibited the presence of both plagioclase (from 5.7 to 17.6 vol. %) and Fe-Ti oxides (from 0.9 to 2.5 vol.%) across the entire experimental range of T investigated (from 1182 to 1131 °C). At the lowest experimental T (1131 °C), clinopyroxene was detected at 4.3 vol.%. In this perspective, it is apparent that high-T_{onset} for the Mt. Etna trachybasalt is likely due to the early crystallization of Fe-Ti oxides, whereas low-T_{onset} for the Stromboli high-K basalt is associated with the crystallization of plagioclase as the *liquidus* phase. This inference is further supported by the experiments carried out at reduced fO_2[27], where the lowest T_{onset} values observed in Fig. 5 can be addressed to suppression of Fe-Ti oxides at reduced fO_2 (this mineral phase is particularly sensitive to low redox conditions) and delayed onset of the plagioclase crystallization at lower T compared to air fO_2 conditions[57]. As observed for the Mt. Etna trachybasaltic melt, a similar trend of delayed crystallization onset of the plagioclase phase (likely with a less marked effect) and, therefore, lower T_{onset} is expected for Stromboli high-K basaltic melt under similarly reduced fO_2 conditions.

Finally, to test the hypothesis of the crystallization of different *liquidus* phases under reduced fO_2 conditions for Mt. Etna melt, we conducted thermodynamic simulations using the MELTS software[58] applying the same fO_2 conditions as those used in the study of Kolzenburg et al.[27] to the Mt.

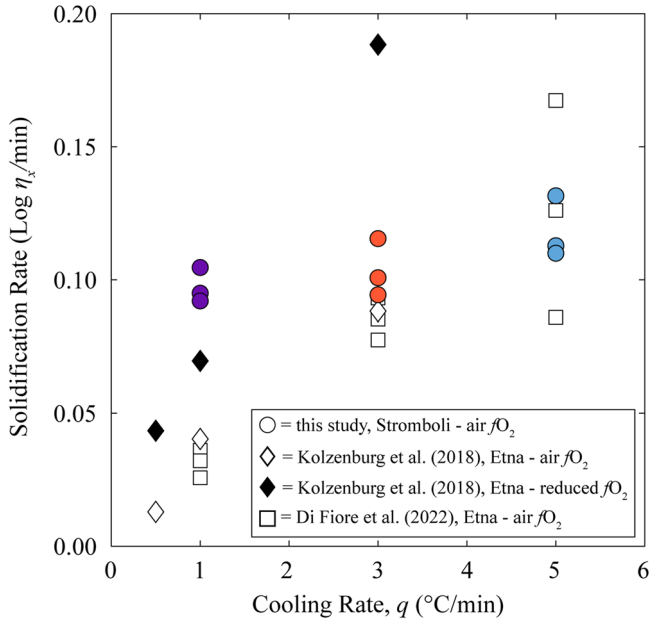

Fig. 6 | Solidification rate values of the Stromboli high-K basaltic melt (this study) and Mt. Etna trachybasaltic melts[27,28] as a function of *q*. Color in the circle symbols (this study) correspond to q of 1 °C/min (purple), 3 °C/min (orange), 5 °C/min (light blue). Error bars are within the symbols. Air fO_2 conditions correspond to log $fO_2 = -0.68$, reduced fO_2 conditions correspond to log $fO_2 = -9.15$.

Etna melt composition. The result of these thermodynamic calculations demonstrated that under air fO_2 conditions, the first phase to crystallize is the Fe-Ti-oxides, while under reduced fO_2 conditions plagioclase is the first phase on *liquidus*.

The distinct phase-in temperatures and crystallization paths of Stromboli and Mt. Etna melts can be attributed to the chemical threshold outlined in a recent study[52]. In this study, a critical compositional factor (specifically, TiO_2 and FeO_{tot} contents) has been identified as a key control on the early - at the nanoscale - crystallization within the compositional domain of basalts. The authors conducted experiments involving the heating of a crystal-free and anhydrous glass from Stromboli and Mt. Etna via DSC measurements, as well as the cooling and decompression of hydrous melts via a piston cylinder apparatus. Their observation of the post-run products revealed that the Mt. Etna melt was highly prone to crystallizing Fe-Ti-bearing nanocrystals (nanolites) in both sets of experiments. Additionally, a comparison of the chemical compositions of the starting materials from Mt. Etna and Stromboli (Supplementary Table 3) showed that Mt. Etna glass compositions contain approximately 1.2 and 1.15 times as much FeO_{tot} (10.94 wt.% and 10.45 wt.% for[27,28]; respectively) compared to the Stromboli composition (9.11 wt.%, this study). Moreover, Mt. Etna composition also features around 2.1 and 1.8 times as much TiO_2 (1.90 wt.% and 1.65 wt.% for[27,28]; respectively) than Stromboli (0.91 wt.%, this study). From a chemical standpoint, these findings provide further confirmation of the early crystallization of Fe-Ti oxides in Mt. Etna melt under air fO_2 conditions, while plagioclase crystallizes from the Stromboli melt.

Another intriguing observation from Fig. 5, by comparing the presented data set with literature data[28], is the similar bilinear relationship between T_{onset} and the variation of q and $\dot{\gamma}$. Both the Stromboli and Mt. Etna melts display a first-order dependency of T_{onset} value on q, while $\dot{\gamma}$ has a second-order impact. Of particular interest is the broader range of T_{onset} values with varying q (within the same experimental range) for the Stromboli high-K basalt (~100 °C, ranging from 1149 to 1049 °C), with respect to the trachybasalt from Mt. Etna (~77 °C, from 1175 to 1098 °C) (Fig. 5a). This heightened sensitivity to q of T_{onset} values for the Stromboli composition is also reflected in the parameter a of Eq. (2), which quantifies the effective influence of q on T_{onset} (expressed as the slope relating to changes in q applied). The value of a from Eq. (2) for Stromboli melt is −1025.12 (± 46.21), while for Mt. Etna is −649.80 (± 25.80)[28]; indicating that the influence of q is roughly 1.6 times smaller for Stromboli compared to Etna. Consequently, the distinct impact of q on the T_{onset} values for these melts also affects the timescales of crystallization (t_{onset}), as derived from Eq. (3).

From Fig. 5b it is evident that $\dot{\gamma}$ exerts a similar influence on T_{onset} in both data sets. As for q, the effective influence of $\dot{\gamma}$ on the T_{onset} values is expressed by the parameter b in Eq. (2). In detail, a comparable effect of $\dot{\gamma}$ on the T_{onset} is observed for both melts, with a variation of about 30 (±2) °C within the range of $\dot{\gamma}$ (i.e., 1–10 s^{-1}) for each applied q. Specifically, the value of b for Stromboli composition is 3.38 (±0.19), while for Mt. Etna is 3.61 (±0.19)[28]. Therefore, it can be concluded that the impact of $\dot{\gamma}$ on the T_{onset} and thus t_{onset} is approximately the same for both these basaltic melts, in contrast to the influence of q. This suggests that the shear rate influence on the crystallization onset is similar for both melts. However, further investigation involving other basaltic compositions (including a broader range of q and $\dot{\gamma}$ and fO_2 conditions) is necessary to enhance our understanding of the effect of these parameters under disequilibrium conditions of crystallization.

Solidification rate

As per the approach utilized in previous CDE studies[26,39,50,59], we calculated the solidification rate from normalized viscosity data (η_x) obtained through CDE. The final η_x values were related to the experimental crystallization time, representing the averaged slope in the η_x–t space.

Figure 6 illustrates the variation in solidification rates concerning the applied q. From Fig. 6, it is evident that both Stromboli and Mt. Etna melts exhibit an increase in solidification rates with increasing q, while the influence of $\dot{\gamma}$ is less pronounced and does not show a clear trend (Supplementary Fig. 3). Crucially, for q lower than 5 °C/min, the Stromboli melt consistently exhibits higher solidification rate than the Mt. Etna melt under the same fO_2 conditions (Fig. 6). This is especially manifested at q of 1 °C/min, where solidification rates of Stromboli are about 2.5–4 times higher than Mt. Etna values deriving from literature[27,28].

Additionally, a delayed crystallization of plagioclase provides explanation for the higher average solidification rate measured for Stromboli melt.

Based on the textural evidence[24], this difference in the solidification rates can be attributed to the various phases that crystallize in these melts. The higher solidification rates observed in Stromboli melt are likely linked to the early crystallization of plagioclase phase. On the other hand, it is well-documented that Mt. Etna melt is more prone to the crystallization of Fe-Ti oxides in both anhydrous and hydrous conditions[24,48,51,52]. The early saturation of Fe-Ti oxides in Etna melts near the *liquidus* temperature observed[24] and predicted by MELTS calculations, likely decreases the extent of plagioclase crystallization and may delay its crystallization onset.

The early crystallization of Fe-Ti oxides could indeed impact the solidification rates for the Mt. Etna melt, resulting in lower values compared to Stromboli melt. This inference is supported by Kolzenburg et al.[27], which explores the rheological solidification pattern of Mt. Etna melt under different fO_2 conditions. In detail, the authors observed a sudden viscosity increase due to crystallization under reduced fO_2, resembling the rheological profiles seen in the Stromboli experiments of this study. Applying the reduced fO_2 conditions adopted by Kolzenburg et al.[27], MELTS calculations indicated that plagioclase is the first phase to crystallize in the Mt. Etna melt. In contrast, for experiments carried out under air fO_2, the authors[27] observed an initial slow increase in viscosity, followed by a rapid viscosity rise. Similar trends in viscosity measurements were observed by Di Fiore et al.[28]. They noted a prolonged region of slow increase of viscosity with increasing $\dot{\gamma}$ at each q, identifying a characteristic timescale that marked the change in the solidification rate of the crystallizing melt. The first region characterized by lower rate of solidification was attributed to shear-induced crystallization and the second region where the higher rate of solidification was predominantly influenced by the cooling rate (Supplementary Fig. 4). The slow

viscosity increase observed by Kolzenburg et al.[27] in CDE under air fO_2 for the Mt. Etna melt aligns with the shear-induced crystallization regime observed in Di Fiore et al.[28]. In both melts the first phase to crystallize under air fO_2 is the Fe-Ti oxides phase.

Based on the comparison of CDE viscosity profiles, textural evidence of the crystallization sequence, and MELTS modelling, it can be inferred that the shear-induced crystallization regime observed for Mt. Etna compositions during CDE under air fO_2 is primarily characterized by the early crystallization of Fe-Ti oxides phases. Subsequently, only at a greater degree of undercooling does the crystallization involve the nucleation of plagioclase and clinopyroxene phases. The slower and earlier crystallization of Fe-Ti oxide phases due to stirring affects the solidification rates under air fO_2 conditions in Mt. Etna melts, resulting in more complex rheological evolution under disequilibrium conditions compared to Stromboli melt.

Finally, to confirm the hypothesis of different rates of solidification due to the early crystallization of different mineral phases, we calculated the solidification rates of the two distinct crystallization regimes identified in the CDE experiments conducted by Di Fiore et al.[28]. The two regimes were reported in Supplementary Table 2. The results depicted illustrate that the solidification rates characterizing the shear-induced regime are consistently lower than the rates associated with the cooling-induced regime (Supplementary Fig. 5). Conversely, the solidification rates linked to the cooling-induced regime are comparable to values derived from experiments conducted under reduced fO_2 and the results of this study (Supplementary Table 2). Therefore, the absence of a shear-induced crystallization region and the similar values of average solidification rates observed for Stromboli and Mt. Etna (under reduced fO_2) experiments suggest the involvement of the same crystallizing phase, namely plagioclase. The sudden increase in viscosity due to plagioclase crystallization contributes to higher solidification rates for both Stromboli and Mt. Etna melts (under reduced fO_2), as opposed to the experiments conducted on Mt. Etna melts under oxidized fO_2 (Fig. 6).

Implications for magma dynamics in basaltic systems

It is well-known that cooling and/or decompression experiments permit investigation of the role of undercooling in syn-eruptive crystallization experienced by magmas during ascent of volcanic conduits or emplacement on the surface[60,61]. In this context, the rheological data presented in this study offer valuable insights into the timescales of solidification for basaltic melts under disequilibrium crystallization conditions. While these experiments are conducted under simplified laboratory conditions (see Supplementary Discussion section), they provide essential information for understanding the combined effects of cooling and shear rate on the rheological evolution of basaltic melts. Comparing our findings with data from previous studies[27,28] permits us to extend our understanding of these factors to the eruptive dynamics of basaltic systems.

We have documented that the cooling rate exerts a stronger influence on the crystallization onset of the Stromboli high-K basalt (i.e., a larger decrease in T_{onset} with increasing q) compared to the Mt Etna trachybasalt. However, both Stromboli and Mt. Etna melts show a similar sensitivity to shear rate (i.e., T_{onset} increases with increasing $\dot{\gamma}$). We infer that these differences are controlled by the different chemical compositions of the melts, particularly transition metal oversaturation, which determine the tendency of Mt. Etna melt to crystallize at higher temperatures and shorter times. Such differences in syn-eruptive crystallization can enhance gas-melt coupling, thus affecting the eruptive styles. As observed in volcanic products from high-explosive basaltic eruptions, the stability of Fe-Ti oxide phases plays a crucial role in the syn-eruptive crystallization stage of magma[9–14,62], acting as preferential nucleation sites for bubbles, thus inhibiting bubble coalescence and enhancing gas-melt coupling[51,63–68]. In this scenario, an increased syn-eruptive crystallization may represent an important contribution to sustained lava fountaining, as in the case of Mt. Etna. In contrast, a melt less prone to crystallize nanolites and microlites of Fe-Ti oxides at the early stage of eruption can result in transient, short-lived explosive paroxysms, as observed at Stromboli.

Another key aspect emerging from CDE data is their ability to experimentally determine the transient (disequilibrium) rheological evolution of basaltic melts, allowing us to quantify the timescales of magma solidification, with important ramifications for the improvement of future numerical modeling studies. To better illustrate the above considerations, we conducted simulations using the solidification rate data obtained from CDE experiments carried out at q of 1, 3 and 5 °C/min and $\dot{\gamma}$ of 10 s^{-1}, showing how the viscosity varies with respect to the time of crystallization in response to different cooling rates for both Stromboli and Mt. Etna melts.

All simulations start at a *superliquidus T* of 1250 °C, representing a state above the melting point for both basaltic melts. The increase of pure liquid viscosity of the melt over time, in response to temperature changes, was calculated using Eq. (1). The onset of crystallization was determined using Eqs. (2) and (3), adopting the parameter values from this study for Stromboli and Di Fiore et al.[28] for Mt. Etna. The black dots in Fig. 7 indicate the T_{onset}, which is consistently lower than the *liquidus* temperature obtained from the MELTS code, reflecting the deviation of our experiments from equilibrium conditions. Below the T_{onset}, the effect of crystallization on viscosity is reproduced according to the solidification rates listed in Supplementary Table 2.

The viscosity is modeled to increase until a fixed value of Log 5 Pa s, representing a critical threshold for the fragmentation of crystal-bearing basaltic magmas[32]. The authors found that the abrupt increase in viscosity, associated with the rapid kinetics of syn-eruptive crystallization, controls the triggering of fragmentation, especially for fast-ascending magma subjected to moderate to high shear rates (between 10^0 and 10^2 s^{-1}) with negligible outgassing phenomena.

The results from simulations, shown in Fig. 7, reveal that both crystallizing melts achieve the fragmentation threshold viscosity in shorter times as the q increases. The timescales required to achieve the threshold viscosity value are comparable for q of 3 and 5 °C/min for the two melts (Supplementary Table 4), even though the T_{onset} of Stromboli are consistently lower than that of Mt. Etna. This difference is due to the fact that the Stromboli magma exhibits a higher solidification rate than the Mt. Etna magma, thus counterbalancing the delayed viscosity increase caused by the onset of crystallization. The latter is linked to the greater sensitivity of Stromboli composition to q (Fig. 5). Focusing on simulations carried out at 1 °C/min, we observe significantly different crystallization timescales for these two basaltic magmas. The Stromboli magma achieves the rheological threshold conditions in 7464 s from the start of the simulation, while the Mt. Etna magma requires 9672 s. Despite the lower T_{onset} of Stromboli, the higher solidification rate after the onset of crystallization leads to a shorter time for the achievement of the rheological threshold, resulting in a 23% reduction in the time needed compared to Mt. Etna. The overriding implication of these simulations is that the integration of different rheological data sets based on compositionally distinct mafic melts is required to fully parameterize the solidification timescales of low-viscosity basalts, particularly for the numerical modeling of volcanic processes.

Considering the natural scenario, in the shallow part of the Stromboli plumbing system, the amount of H_2O dissolved in the melt decreases from ~2.4 to ~0.5 wt.% over a decompression path of 100 MPa[69–72]. Assuming H_2O saturation in the melt, the exsolution of H_2O from the melt determines an increase in *liquidus* temperature of ~25 °C. Since the ascent rate of magma is ~240–600 m/min[71,73], we found that cooling rates of ~2–4 °C/min (such as those used in this study) correspond to decompression rates ~6–16 MPa/min. In natural scenarios, however, a range of processes control both the magma crystallization and degassing, this latter phenomenon assumed as negligible for our simplified experimental approach. As a consequence, magma decompression and volatile exsolution can concurrently take place with cooling phenomena caused by adiabatic expansion. These mutual effects may produce a certain amount of disequilibrium that can be expressed in terms of supersaturation for each crystallizing mineral phase[74,75]. The supersaturation condition can be quantified as the difference between the equilibrium and the actual crystal fraction of the considered mineral

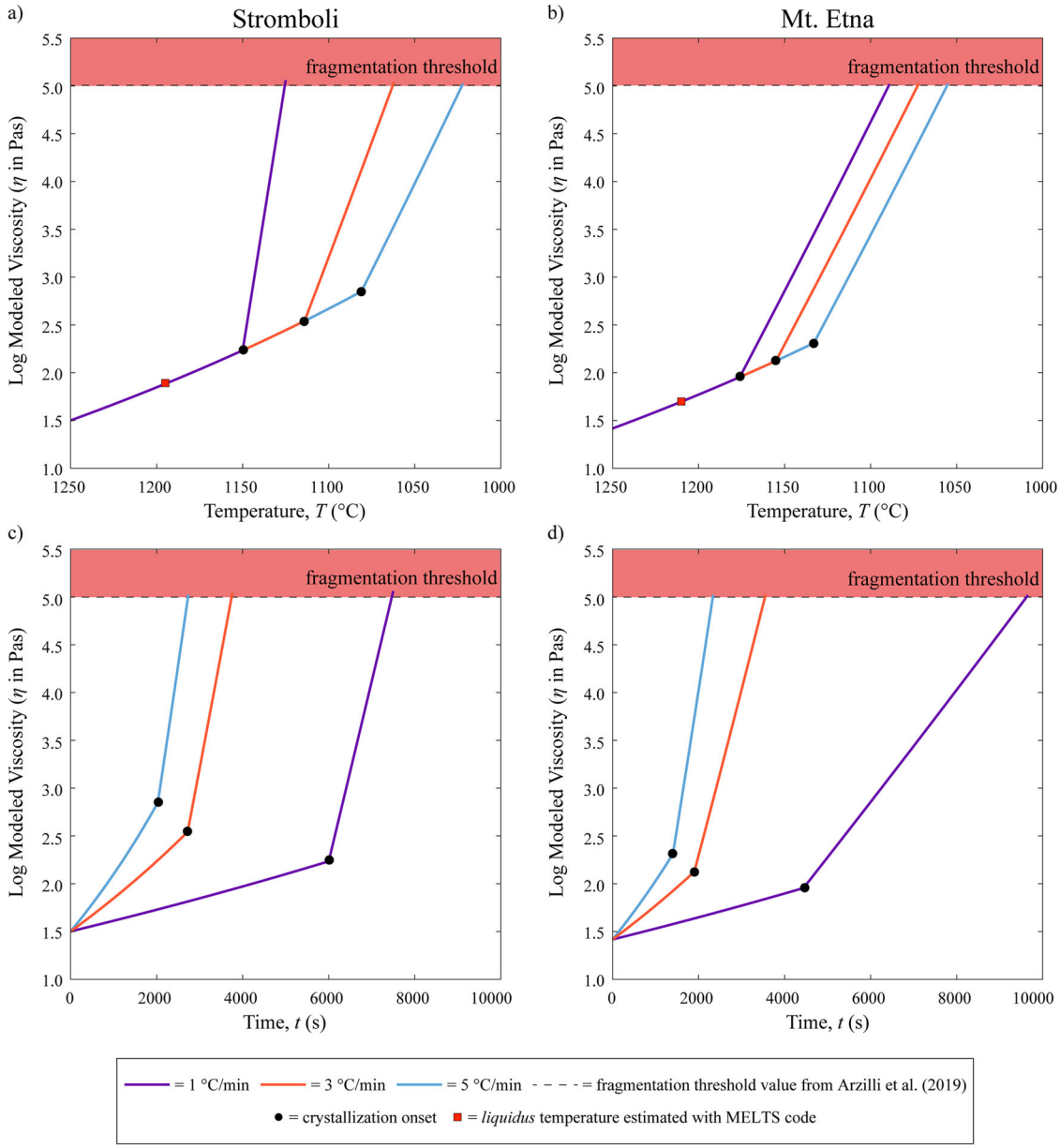

Fig. 7 | Numerical modeling of the solidification *T* and *t* for Stromboli high-K basaltic melt and Mt. Etna trachybasaltic melts. Results of numerical modeling show the viscosity evolution as a function of temperature and time calculated for different q (i.e., 1-3-5 °C/min) and constant $\dot{\gamma}$ (i.e., 10 s^{-1}) for the Stromboli high-K basaltic melt (**a**–**c**, this study) and the Mt. Etna trachybasaltic melt (**b**–**d**)[28].

phase at a given temperature–pressure condition[75], thereby giving a more robust estimate for the cooling and decompression paths of magmas.

This aspect highlights the necessity to improve our capability of sampling the post-experimental run of CDE for future studies. This will permit to focus future studies aimed at parametrizing the effects of both cooling and decompression rates (and also on the shear rate) on the supersaturation of the crystallizing phases in the melt, improving our knowledge on their role and their complex interplay during volcanic eruption.

Conclusions

Cooling Deformation Experiments (CDE) from this study are combined with Isothermal Deformation Experiments (IDE) from literature to define a thermo-rheological space for disequilibrium (CDE) and near-equilibrium (IDE) crystallization of a high-K basalt erupted at Stromboli. To offer a more holistic view of the rheological evolution of basaltic magmas, this new dataset has been also compared with different datasets of trachybasaltic melts from Mt. Etna. Based on this integrated experimental and comparative approach, the following conclusions can be drawn:

- the effect of cooling rate predominantly controls the crystallization onset of the Stromboli melt, while the shear rate plays a secondary role, becoming more effective at slower cooling rates.
- the crystallization onset of the Stromboli melt can be parameterized through a bilinear function that considers the effects of cooling rate and shear rate under dynamic solidification conditions. Specifically, higher cooling rates result in lower crystallization temperatures and shorter times, while increased shear rates lead to higher temperatures and faster crystallization onset;
- the shear rate exerts similar effects on the crystallization onset of both melts from Stromboli and Mt. Etna, whereas the cooling rate has a more pronounced impact on the crystallization onset of the Stromboli melt;
- at *subliquidus* temperatures, the early saturation of distinct mineral phases under air oxygen fugacity conditions for both high-K basalt from Stromboli (plagioclase) and the trachybasalts from Mt. Etna (Fe-Ti

oxides) causes differences in the timescales of crystallization onset and solidification rate for the two magmas, in response to a compositional threshold that is mainly controlled by the variable proportions of TiO_2 and FeO_{tot} in the bulk rock compositions;
- by extrapolating our experimentally-derived rheological parameterization to natural eruptive scenarios, it is postulated that the change of crystallization timescale between these two basaltic melts may influence magma degassing dynamics, thereby modulating the eruptive behavior at Stromboli and Mt. Etna.

Material and methods

Starting material, sample preparation, and chemical analysis

As starting material we used a high-K basalt pumice lapilli erupted from Stromboli volcano (Italy) during the paroxysmal event of April 5, 2003 (e.g. ref. 76). The pumices were crushed into a fine powder using a jaw crusher and a ring mill. The resulting powder was melted in a Fe-presatured Pt crucible using a Naberthern® furnace at 1400 °C. The molten material was kept at a constant temperature for ~3 h and afterwards rapidly quenched to a glass. Two cycles of melting and quenching were carried out to guarantee the melt homogenization. Subsequently, a portion of the glass obtained was re-melted into a Fe-presaturated $Pt_{80}Rh_{20}$ cylindric crucible for high-temperature (high-*T*) viscometry measurements using a concentric cylinder apparatus. Shards of glass chips were utilized for the heat flow measurements and for the chemical characterization of the sample. The chemical composition of the analyzed glass, along with the associated error, is presented as oxide concentrations in Table 3. The chemical analysis was carried out using a Jeol-JXA8200 electron microprobe equipped with five wavelength dispersive spectrometers at the High Pressures – High Temperatures Laboratory of Experimental Volcanology and Geophysics (HP-HT Lab) of the Istituto Nazionale di Geofisica e Vulcanologia in Rome (Italy). Analytical conditions are reported in the Supplementary Methods (1).

The MELTS code[58] was employed to estimate the *liquidus* temperature of the melt ($T_{liquidus}$ of 1195 °C) at 1 atm and air redox condition, using as input data the major oxide concentrations listed in Table 3.

High-*T* liquid viscosity

High-*T* viscosity measurements were carried out using a Concentric Cylinder (CC) apparatus at the Laboratory of Experimental Volcanology and Petrology (EVPLab) of Roma Tre University. The CC setup includes a Rheotronic II Rotational Viscometer (Theta Instruments) with an Anton Paar Rheolab Qc viscometer head (full-scale torque of 75 mNm), an S-type thermocouple (with an accuracy of ±2 °C), a Fe-presaturated $Pt_{80}Rh_{20}$ cylindric crucible (62, 32, and 1.5 mm in height, inner diameter, and wall thickness, respectively) and a Fe-presaturated $Pt_{80}Rh_{20}$ spindle (3.2 and 42 mm in diameter and length, respectively). The temperature of the sample is constantly monitored with an S-type thermocouple ubicated in close proximity to the crucible wall. The calibration procedure and precision of the CC apparatus are reported in detail in the Supplementary Method section. The glassy material previously charged in the cylindric crucible was re-heated to a *superliquidus* temperature of 1400 °C at a rate of 30 °C/min. Once a temperature of 1400 °C was reached, the sample was stirred at a constant shear rate ($\dot{\gamma}$) of 10 s^{-1}, under ambient pressure (i.e., 1 atm) and air redox conditions (i.e., log fO_2 of −0.68) for a duration of ~3 h, in order to ensure the thermal and the chemical homogenization of the melt. Subsequently, the furnace temperature was gradually reduced to reach the desired target *T*: 1350 – 1325 – 1300 – 1275 – 1250 °C. The apparent viscosity (η_a) of the sample at each *T* is calculated as follows:

$$\eta_a = \frac{\tau}{\dot{\gamma}} \tag{4}$$

where τ is the shear stress (in Pa) and it is determined by the measured torque at the inner cylinder and $\dot{\gamma}$ is the shear rate applied (in s^{-1}). For each *T*, the apparent viscosity (η_a) of the melt was measured until a stable torque and temperature were reached (~45 min).

Low-*T* liquid viscosity

The melt viscosity at low temperature was derived using Differential Scanning Calorimetry (DSC) measurements. This technique deals with the structural relaxation process occurring at the glass transition interval by examining the heat flow signal of the glass under controlled temperature.

The use of DSC to derive viscosity relies on the close relationship between structural and stress relaxation times in glass melts. This means that the processes governing changes in the structural arrangement of the melt also govern its response to stress. The activation energy for viscous flow can be closely approximated by the activation energy for structural relaxation calculated from DSC data. This allows us to indirectly determine viscosity from the thermal behavior observed during DSC measurements. A literature review of this approach has been recently provided by Stabile et al.[77].

Analysis of the DSC traces yields two characteristic temperatures: the onset temperature of the glass transition (T_{onset}) and the peak temperature of the glass transition (T_{peak}). By applying a parallel shift factor (K[51,78–80]), the non-Arrhenian dependence of T_{onset} and T_{peak} on cooling rate (q) can be overlaid on the non-Arrhenian temperature dependence viscosity (η)[77]and reference therein). Consequently, T_{onset} and T_{peak} can be associated with melt viscosity values using the following equation:

$$Log\ \eta\left(T^{DSC}_{onset,peak}\right) = K_{onset,peak} - Log(|q|) \tag{5}$$

where q is expressed in K/s. The DSC measurements were carried out on shards of the previously synthesized Stromboli glass (20 ± 5 mg) using a Netzsch Pegasus 404 DSC. These measurements were performed in $PtRh_{20}$ crucibles under N_2 at 5.0 atm with a flow rate of 25 – 80 ml/min. Samples were subjected to matching cooling and heating rates of 10 and 20 K/min. For a detailed calibration procedure see Scarani et al. [52]. The parallel shift factor values used to obtain viscosity values were obtained by Di Genova et al. [51] (i.e., K_{onset} = 11.20 and K_{peak} = 9.78). The absence of crystals in the pre- and post-run glasses was checked by Raman spectroscopy analyses.

Cooling deformation experiments

All Cooling Deformation Experiments (CDE) were carried out on the same CC apparatus employed for the high-*T* viscosity characterization. The *superliquidus* treatment (i.e., pre-experiment melt homogenization) was carried out by stirring the melt at 10 s^{-1} and 1400 °C until the viscosity value, as measured during high-*T* viscosity measurement assessment, was recovered (~3 h). This procedure ensured the thorough dissolution of any potential crystalline nuclei present in the melt.

CDE were carried out at constant cooling rate (q) of 1, 3, 5 and 10 °C/min. For each q of 1, 3 and 5 °C/min, three runs were executed, employing shear rate ($\dot{\gamma}$) values of 1, 5, and 10 s^{-1}. Only a $\dot{\gamma}$ of 10 s^{-1} was employed for q of 10 °C/min. The range of q and $\dot{\gamma}$ adopted in this study correspond to a relevant part of the wider range of the dynamic conditions associated with natural processes spanning from magma migration through the Earth's crust to the emplacement of lava flow on the Earth's surface. Specifically, the measured and modeled q experienced by a basaltic magma during its ascent in a volcanic conduit and emplacement as a lava flow span from 0.01 to 20 °C/min[6,39,50,81,82]. Furthermore, the shear rates experienced by magma during viscous transport within volcanic systems may vary from a maximum of 7×10^1 s^{-1} during Plinian eruptions[83] to 10^1–10^{-3} s^{-1} during the emplacement of mafic lava flows[47,50,84,85], down to 10^{-9} s^{-1} in convecting magma chambers[86,87].

The experiments were halted manually to protect the apparatus from the high shear rate and stress imposed. The apparent viscosity threshold values at which the experiments were interrupted depended on the applied shear rate and were approximately $10^{4.5}$, $10^{3.8}$, and $10^{3.5}$ Pa s for $\dot{\gamma}$ of 1, 5 and 10 s^{-1}, respectively. These viscosity values represented a fixed threshold value of shear stress of $10^{4.5}$ Pa. Obtaining representative textures of the post-run products in CDE that accurately reflect the applied experimental conditions is technically challenging due to the significant undercooling, rapid

chemical diffusion, and fast crystallization kinetics characteristic of low-η melts, such as basalt. This is attributed to the continued crystallization during the time required for spindle removal and sample quenching. In detail, the time required to extract the spindle from the sample ranges from ~4 to ~8 min with increasing viscosity reached during the experiments (from $10^{3.5}$ to $10^{4.5}$ Pa s). In addition, a timespan of ~6–8 min is necessary for quench the sample by holding the crucible walls under a water flow (an average rate of cooling of ~120 °C/min[39]). Therefore, no post-run samples are available, and after each CDE run, the sample was re-heated and was subjected to a new cycle of *superliquidus* treatment before starting a new experimental measurement. At the end of the last cycle, an additional *superliquidus* treatment was carried out to quench the melt to glass, to verify that no alkali and iron loss occurred, as outlined by the re-analyzed glass composition reported in Table 3.

Normalized viscosity

The absence of post-run analyses represents the major limitation of CDE procedure, while the classical Isothermal Deformation Experiments (IDE[24,35,39,49,59,88–93]), permit the quantification of textural and chemical features of the post-run experiment (Supplementary Fig. 2).

The achievement of a stable crystal content in IDE permits to quench the sample and obtain post-run sample representative of the experimental conditions. This aspect enables the determination of the relative viscosity (i.e., the net effect of crystals, η_r) with respect to the apparent viscosity (i.e., the viscosity of the suspension η_a) through image and chemical analysis on post-run samples. These post-run analyses permit to quantify the content of crystals, which plays a crucial role in increasing magma viscosity with increasing crystal volume fraction[94,95], and the estimation of viscosity of the residual glass (η_{res}) using empirical and chemically-based viscosity models[23,44].

The η_r can be estimated by the ratio of apparent viscosity to residual melt viscosity:

$$\eta_r = \frac{\eta_a}{\eta_{res}} \tag{6}$$

Conversely, CDE setup only accounts for the combined impact of crystallization (i.e., both physical and chemical impact) on the apparent viscosity, as it is not possible to distinguish between the physical (the increasing amount of solid phases; i.e., crystals) and chemical (i.e., changes of the residual melt compositions) contributions to magma viscosity. Recent studies[28,47] introduced the concept of normalized viscosity (η_x) to account for both the physical and chemical effects of crystallization on viscosity evolution. In particular for mafic compositions, it is known that the chemical effect of the residual liquid on viscosity evolution is typically secondary for crystal contents up to 40%, as estimated for the variation of viscosity by Vona et al. [24] for Stromboli high-K basalt ($10^{0.08–0.10}$ Pa s) and by Vona et al.[24] and Kolzenburg et al.[96] for Mt. Etna trachybasalt ($10^{0.06–0.18}$ and $10^{0.03}$ Pa s, respectively). In this study, we employ this approach by normalizing each CDE's η_a with the pure liquid viscosity (η_{liquid}) of the starting melt composition:

$$\eta_x = \frac{\eta_a}{\eta_{liquid}} \tag{7}$$

where η_x is the normalized viscosity. The onset of crystallization is identified in correspondence to a $10^{0.05}$ Pa s increase in η_x, which is followed by a monotonic positive upward trend[28,47]. This increase in viscosity corresponds to a crystal content that can be retrieved by using empirical models[24,95] that account for the effect of crystals on the suspension in relation to the mean aspect ratio of the crystals (i.e., the elongation of the particles) and the shear rate applied. Results show that the crystal contents span from 2.3 % to 3.3% for crystal aspect ratio spanning between 1 and 6, and shear rates ranging from 1 to 10 s^{-1} (see Supplementary Table 1 for a detailed estimation of the crystal content related to the different aspect ratio and shear rate).

Data availability

The raw data used for this study are available online at the following link: https://doi.org/10.6084/m9.figshare.24849492.v1

Received: 26 December 2023; Accepted: 17 May 2024;
Published online: 27 May 2024

References

1. Parfitt, E. A. A discussion of the mechanisms of explosive basaltic eruptions. *J. Volcanol. Geotherm. Res.* **134**, 77–107 (2004).
2. Braden, S. E. et al. Evidence for basaltic volcanism on the Moon within the past 100 million years. *Nat. Geosci.* **7**, 787–791 (2014).
3. Byrne, P. K. A comparison of inner Solar System volcanism. *Nat. Astron.* **4**, 321–327 (2020).
4. Houghton, B. F. & Gonnermann, H. M. Basaltic explosive volcanism: Constraints from deposits and models. *Chemie Der Erde* **68**, 117–140 (2008).
5. Gonnermann, H. M. et al. Permeability During Magma Expansion and Compaction. *J. Geophys. Res. Solid Earth* **122**, 9825–9848 (2017).
6. La Spina, G., Burton, M., de' Michieli Vitturi, M. & Arzilli, F. Role of syn-eruptive plagioclase disequilibrium crystallization in basaltic magma ascent dynamics. *Nat. Commun.* **7**, 13402 (2016).
7. La Spina, G. et al. Explosivity of basaltic lava fountains is controlled by magma rheology, ascent rate and outgassing. *Earth Planet. Sci. Lett.* **553**, 116658 (2021).
8. Namiki, A., Patrick, M. R., Manga, M. & Houghton, B. F. Brittle fragmentation by rapid gas separation in a Hawaiian fountain. *Nat. Geosci.* **14**, 242–247 (2021).
9. Coltelli, M., Del Carlo, P. & Vezzoli, L. Discovery of a Plinian basaltic eruption of Roman age at Etna volcano, Italy. *Geology* **26**, 1095–1098 (1998).
10. Szramek, L. A. Mafic Plinian eruptions: Is fast ascent required? *J. Geophys. Res. Solid Earth* **121**, 7119–7136 (2016).
11. Rowe, M. C. et al. Tarawera 1886: an integrated review of volcanological and geochemical characteristics of a complex basaltic eruption. *New Zeal. J. Geol. Geophys.* **64**, 296–319 (2021).
12. Valdivia, P., Marshall, A. A., Brand, B. D., Manga, M. & Huber, C. Mafic explosive volcanism at Llaima Volcano: 3D x-ray microtomography reconstruction of pyroclasts to constrain shallow conduit processes. *Bull. Volcanol.* **84**, 2 (2022).
13. Costantini, L., Houghton, B. F. & Bonadonna, C. Constraints on eruption dynamics of basaltic explosive activity derived from chemical and microtextural study: The example of the Fontana Lapilli Plinian eruption, Nicaragua. *J. Volcanol. Geotherm. Res.* **189**, 207–224 (2010).
14. Bamber, E. C. et al. Pre- and syn-eruptive conditions of a basaltic Plinian eruption at Masaya Volcano, Nicaragua: The Masaya Triple Layer (2.1 ka). *J. Volcanol. Geotherm. Res.* **392**, 106761 (2020).
15. Mueller, S., Scheu, B., Spieler, O. & Dingwell, D. B. Permeability control on magma fragmentation. *Geology* **36**, 399–402 (2008).
16. Cashman, K. V. & Scheu, B. Magmatic Fragmentation. In *The Encyclopedia of Volcanoes* 459–471 (Elsevier, 2015). https://doi.org/10.1016/B978-0-12−385938-9.00025-0.
17. Cassidy, M., Manga, M., Cashman, K. & Bachmann, O. Controls on explosive-effusive volcanic eruption styles. *Nat. Commun*. **9**, 2839 (2018).
18. Jones, T. J., Cashman, K. V., Liu, E. J., Rust, A. C. & Scheu, B. Magma fragmentation: a perspective on emerging topics and future directions. *Bull. Volcanol.* **84**, 45 (2022).
19. Kobayashi, M., Okumura, S., Sasaki, O. & de Silva, S. L. The role of decompression history in gas bubble formation in crystal-rich silicic

magma: Gas retention versus segregation. *J. Volcanol. Geotherm. Res.* **439**, 107844 (2023).
20. Shea, T. Bubble nucleation in magmas: A dominantly heterogeneous process? *J. Volcanol. Geotherm. Res.* **343**, 155–170 (2017).
21. Cáceres, F. et al. The roles of microlites and phenocrysts during degassing of silicic magma. *Earth Planet. Sci. Lett.* **577**, 117264 (2022).
22. Gardner, J. E. et al. Bubble Formation in Magma. *Annu. Rev. Earth Planet. Sci.* **51**, 131–154 (2023).
23. Giordano, D., Russell, J. K. & Dingwell, D. B. Viscosity of magmatic liquids: A model. *Earth Planet. Sci. Lett.* **271**, 123–134 (2008).
24. Vona, A., Romano, C., Dingwell, D. B. & Giordano, D. The rheology of crystal-bearing basaltic magmas from Stromboli and Etna. *Geochim. Cosmochim. Acta* **75**, 3214–3236 (2011).
25. Kolzenburg, S., Giordano, D., Cimarelli, C. & Dingwell, D. B. In situ thermal characterization of cooling/crystallizing lavas during rheology measurements and implications for lava flow emplacement. *Geochim. Cosmochim. Acta* **195**, 244–258 (2016).
26. Kolzenburg, S., Hess, K. U., Berlo, K. & Dingwell, D. B. Disequilibrium Rheology and Crystallization Kinetics of Basalts and Implications for the Phlegrean Volcanic District. *Front. Earth Sci.* **8**, 187 (2020).
27. Kolzenburg, S., Di Genova, D., Giordano, D., Hess, K. U. & Dingwell, D. B. The effect of oxygen fugacity on the rheological evolution of crystallizing basaltic melts. *Earth Planet. Sci. Lett.* **487**, 21–32 (2018).
28. Di Fiore, F., Vona, A., Costa, A., Mollo, S. & Romano, C. Quantifying the influence of cooling and shear rate on the disequilibrium rheology of a trachybasaltic melt from Mt. Etna. *Earth Planet. Sci. Lett.* **594**, 117725 (2022).
29. Vona, A., Romano, C., Giordano, G. & Sulpizio, R. Linking magma texture, rheology and eruptive style during the 472 AD Pollena Subplinian eruption (Somma-Vesuvius). *Lithos* **370–371**, 105658 (2020).
30. Gonnermann, H. M. Magma Fragmentation. *Annu. Rev. Earth Planet. Sci.* **43**, 431–458 (2015).
31. Moitra, P., Gonnermann, H. M., Houghton, B. F. & Tiwary, C. S. Fragmentation and Plinian eruption of crystallizing basaltic magma. *Earth Planet. Sci. Lett.* **500**, 97–104 (2018).
32. Arzilli, F. et al. Magma fragmentation in highly explosive basaltic eruptions induced by rapid crystallization. *Nat. Geosci.* **12**, 1023–1028 (2019).
33. Arzilli, F. et al. Dendritic crystallization in hydrous basaltic magmas controls magma mobility within the Earth's crust. *Nat. Commun.* **13**, 3354 (2022).
34. Kouchi, A., Tsuchiyama, A. & Sunagawa, I. Effect of stirring on crystallization kinetics of basalt: texture and element partitioning. *Contrib. Mineral. Petrol.* **93**, 429–438 (1986).
35. Chevrel, M. O. et al. Viscosity measurements of crystallizing andesite from Tungurahua volcano (Ecuador). *Geochemistry*. *Geophys. Geosyst.* **16**, 870–889 (2015).
36. Chevrel, M. O. et al. The viscosity of pāhoehoe lava: In situ syn-eruptive measurements from Kilauea, Hawaii. *Earth Planet. Sci. Lett.* **493**, 161–171 (2018).
37. Rusiecka, M. K., Bilodeau, M. & Baker, D. R. Quantification of nucleation delay in magmatic systems: experimental and theoretical approach. *Contrib. Mineral. Petrol.* **175**, 47 (2020).
38. Taddeucci, J. et al. Fracturing and healing of basaltic magmas during explosive volcanic eruptions. *Nat. Geosci.* **14**, 248–254 (2021).
39. Di Fiore, F., Vona, A., Kolzenburg, S., Mollo, S. & Romano, C. An Extended Rheological Map of Pāhoehoe—'A'ā Transition. *J. Geophys. Res. Solid Earth* **126**, 1–23 (2021).
40. Polacci, M. et al. Crystallisation in basaltic magmas revealed via in situ 4D synchrotron X-ray microtomography. *Sci. Rep.* **8**, 8377 (2018).
41. Pontesilli, A. et al. Crystallization kinetics of clinopyroxene and titanomagnetite growing from a trachybasaltic melt: New insights from isothermal time-series experiments. *Chem. Geol.* **510**, 113–129 (2019).
42. Masotta, M. et al. The role of undercooling during clinopyroxene growth in trachybasaltic magmas: Insights on magma decompression and cooling at Mt. Etna volcano. *Geochim. Cosmochim. Acta* **268**, 258–276 (2020).
43. Le Gall, N. et al. In situ quantification of crystallisation kinetics of plagioclase and clinopyroxene in basaltic magma: Implications for lava flow. *Earth Planet. Sci. Lett.* **568**, 117016 (2021).
44. Langhammer, D., Di Genova, D. & Steinle-Neumann, G. Modeling Viscosity of Volcanic Melts With Artificial Neural Networks. *Geochem. Geophys. Geosyst.* **23**, 1–14 (2022).
45. Giordano, D. et al. Thermo-rheological magma control on the impact of highly fluid lava flows at Mt. Nyiragongo. *Geophys. Res. Lett.* **34**, 2–5 (2007).
46. Vetere, F. et al. Glass forming ability and crystallisation behaviour of sub-alkaline silicate melts. *Earth Sci. Rev.* **150**, 25–44 (2015).
47. Di Fiore, F. et al. Experimental Constraints on the Rheology of Lavas From 2021 Cumbre Vieja Eruption (La Palma, Spain). *Geophys. Res. Lett*. **50**, e2022GL100970 (2023).
48. Vona, A. & Romano, C. The effects of undercooling and deformation rates on the crystallization kinetics of Stromboli and Etna basalts. *Contrib. Mineral. Petrol.* **166**, 491–509 (2013).
49. Di Fiore, F. et al. Kinetic partitioning of major and trace cations between clinopyroxene and phonotephritic melt under convective stirring conditions: New insights into clinopyroxene sector zoning and concentric zoning. *Chem. Geol.* **584**, 120531 (2021).
50. Kolzenburg, S., Chevrel, M. O., Dingwell, D. B. & Hall, C. Magma/Suspension Rheology. *Rev. Mineral. Geochem.* **87**, 639–720 (2022).
51. Di Genova, D. et al. In situ observation of nanolite growth in volcanic melt: A driving force for explosive eruptions. *Sci. Adv.* **6**, eabb0413 (2020).
52. Scarani, A. et al. A chemical threshold controls nanocrystallization and degassing behaviour in basalt magmas. *Commun. Earth Environ.* **3**, 284 (2022).
53. Valdivia, P. et al. Are volcanic melts less viscous than we thought? The case of Stromboli basalt. *Contrib. Mineral. Petrol.* **178**, 45 (2023).
54. First, E. C., Leonhardi, T. C. & Hammer, J. E. Effects of superheating magnitude on olivine growth. *Contrib. Mineral. Petrol.* **175**, 13 (2020).
55. Auxerre, M., Faure, F. & Lequin, D. The effects of superheating and cooling rate on olivine growth in chondritic liquid. *Meteorit. Planet. Sci.* **57**, 1474–1495 (2022).
56. Vona, A., Romano, C., Giordano, D. & Russell, J. K. The multiphase rheology of magmas from Monte Nuovo (Campi Flegrei, Italy). *Chem. Geol.* **346**, 213–227 (2013).
57. Burkhard, D. J. M. & Scherer, T. The effect of initial oxidation state on crystallization of basaltic glass. *J. Non. Cryst. Solids* **352**, 3961–3969 (2006).
58. Ghiorso, M. S. & Sack, R. O. Chemical mass transfer in magmatic processes IV. A revised and internally consistent thermodynamic model for the interpolation and extrapolation of liquid-solid equilibria in magmatic systems at elevated temperatures and pressures. *Contrib. Mineral. Petrol.* **119**, 197–212 (1995).
59. Di Fiore, F. et al. Experimental insights on the shear-induced crystallization of a phonotephrite magma. *Chem. Geol.* **637**, 121682 (2023).
60. Shea, T. & Hammer, J. E. Kinetics of cooling- and decompression-induced crystallization in hydrous mafic-intermediate magmas. *J. Volcanol. Geotherm. Res.* **260**, 127–145 (2013).
61. Mollo, S. & Hammer, J. E. Dynamic crystallization in magmas. In *Mineral reaction kinetics: Microstructures, textures, chemical and isotopic signatures* 16, 378–418 (Mineralogical Society of Great Britain & Ireland, 2017).

62. Marshall, A. A. et al. The mafic Curacautín ignimbrite of Llaima volcano, Chile. *J. Volcanol. Geotherm. Res.* **421**, 107418 (2022).
63. Di Genova, D., Caracciolo, A. & Kolzenburg, S. Measuring the degree of "nanotilization" of volcanic glasses: Understanding syn-eruptive processes recorded in melt inclusions. *Lithos* **318–319**, 209–218 (2018).
64. Pleše, P. et al. Production and detachment of oxide crystal shells on bubble walls during experimental vesiculation of andesitic magmas. *Contrib. Mineral. Petrol.* **174**, 1–20 (2019).
65. Knipping, J. L., Webster, J. D., Simon, A. C. & Holtz, F. Accumulation of magnetite by flotation on bubbles during decompression of silicate magma. *Sci. Rep.* **9**, 1–7 (2019).
66. Cáceres, F. et al. Can nanolites enhance eruption explosivity? *Geology* **48**, 997–1001 (2020).
67. Cáceres, F. et al. From melt to crystals: The effects of cooling on Fe Ti oxide nanolites crystallisation and melt polymerisation at oxidising conditions. *Chem. Geol.* **563**, 120057 (2021).
68. Yoshida, K. et al. Oxidation-induced nanolite crystallization triggered the 2021 eruption of Fukutoku-Oka-no-Ba. *Japan. Sci. Rep.* **13**, 1–9 (2023).
69. Métrich, N., Bertagnini, A. & Di Muro, A. Conditions of magma storage, degassing and ascent at Stromboli: New insights into the volcano plumbing system with inferences on the eruptive dynamics. *J. Petrol.* **51**, 603–626 (2009).
70. Di Stefano, F. et al. Mush cannibalism and disruption recorded by clinopyroxene phenocrysts at Stromboli volcano: New insights from recent 2003–2017 activity. *Lithos* **360–361**, 105440 (2020).
71. Moschini, P. et al. A review of plagioclase growth rate and compositional evolution in mafic alkaline magmas: Guidelines for thermometry, hygrometry, and timescales of magma dynamics at Stromboli and Mt. Etna. *Earth Sci. Rev.* **240**, 104399 (2023).
72. Voloschina, M. et al. Explosive eruptions at Stromboli volcano (Italy): a comprehensive geochemical view on magma sources and intensity range. *Bull. Volcanol.* **85**, 34 (2023).
73. Le Gall, N. & Pichavant, M. Experimental simulation of bubble nucleation and magma ascent in basaltic systems: Implications for Stromboli volcano. *Am. Mineral.* **101**, 1967–1985 (2016).
74. Befus, K. S. & Andrews, B. J. Crystal nucleation and growth produced by continuous decompression of Pinatubo magma. *Contrib. Mineral. Petrol.* **173**, 92 (2018).
75. Andrews, B. J. & Befus, K. S. Supersaturation Nucleation and Growth of Plagioclase: a numerical model of decompression-induced crystallization. *Contrib. Mineral. Petrol.* **175**, 1–20 (2020).
76. Pontesilli, A. et al. Magma Differentiation in Dynamic Mush Domains From the Perspective of Multivariate Statistics: Open- Versus Closed-System Evolution. *Geochem. Geophys. Geosyst.* **25**, 1–20 (2024).
77. Stabile, P. et al. The effect of iron and alkali on the nanocrystal-free viscosity of volcanic melts: A combined Raman spectroscopy and DSC study. *Chem. Geol.* **559**, 119991 (2021).
78. Stevenson, R. J., Dingwell, D. B., Webb, S. L. & Bagdassarov, N. S. The equivalence of enthalpy and shear stress relaxation in rhyolitic obsidians and quantification of the liquid-glass transition in volcanic processes. *J. Volcanol. Geotherm. Res.* **68**, 297–306 (1995).
79. Gottsmann, J. & Dingwell, D. B. The thermal history of a spatter-fed lava flow: the 8-ka pantellerite flow of Mayor Island, New Zealand. *Bull. Volcanol.* **64**, 410–422 (2002).
80. Giordano, D., Potuzak, M., Romano, C., Dingwell, D. B. & Nowak, M. Viscosity and glass transition temperature of hydrous melts in the system CaAl2Si2O8–CaMgSi2O6. *Chem. Geol.* **256**, 203–215 (2008).
81. Hon, K., Kauahikaua, J., Denlinger, R. & Mackay, K. Emplacement and inflation of pahoehoe sheet flows: Observations and measurements of active lava flows on Kilauea Volcano, Hawaii. *Geol. Soc. Am. Bull.* **106**, 351–370 (1994).
82. Cashman, K. V., Thornber, C. & Kauahikaua, J. P. Cooling and crystallization of lava in open channels, and the transition of Pāhoehoe Lava to'A'ā. *Bull. Volcanol.* **61**, 306–323 (1999).
83. Papale, P. Strain-induced magma fragmentation in explosive eruptions. *Nature* **397**, 425–428 (1999).
84. Harris, A. J. L. & Rowland, S. K. Lava Flows and Rheology. In *The Encyclopedia of Volcanoes* (ed. Sigurdsson. H.) 321–342 (Elsevier, 2015). https://doi.org/10.1016/B978-0-12-385938-9.00017-1.
85. Harris, A. et al. How shear helps lava to flow. *Geology* **48**, 154–158 (2020).
86. Huber, C., Bachmann, O. & Manga, M. Homogenization processes in silicic magma chambers by stirring and mushification (latent heat buffering). *Earth Planet. Sci. Lett.* **283**, 38–47 (2009).
87. Bachmann, O. & Huber, C. Silicic magma reservoirs in the Earth's crust. *Am. Mineral.* **101**, 2377–2404 (2016).
88. Vetere, F., Mazzeo, A., Perugini, D. & Holtz, F. Viscosity behaviour of silicate melts during cooling under variable shear rates. *J. Non. Cryst. Solids* **533**, 119902 (2020).
89. Ishibashi, H. & Sato, H. Viscosity measurements of subliquidus magmas: Alkali olivine basalt from the Higashi-Matsuura district, Southwest Japan. *J. Volcanol. Geotherm. Res.* **160**, 223–238 (2007).
90. Vetere, F., Sato, H., Ishibashi, H., De Rosa, R. & Donato, P. Viscosity changes during crystallization of a shoshonitic magma: new insights on lava flow emplacement. *J. Mineral. Petrol. Sci.* **108**, 144–160 (2013).
91. Sehlke, A. et al. Pahoehoe to 'a'a transition of Hawaiian lavas: an experimental study. *Bull. Volcanol.* **76**, 876 (2014).
92. Campagnola, S., Vona, A., Romano, C. & Giordano, G. Crystallization kinetics and rheology of leucite-bearing tephriphonolite magmas from the Colli Albani volcano (Italy). *Chem. Geol.* **424**, 12–29 (2016).
93. Soldati, A., Sehlke, A., Chigna, G. & Whittington, A. Field and experimental constraints on the rheology of arc basaltic lavas: the January 2014 Eruption of Pacaya (Guatemala). *Bull. Volcanol.* **78**, 43 (2016).
94. Costa, A., Caricchi, L. & Bagdassarov, N. A model for the rheology of particle-bearing suspensions and partially molten rocks. *Geochem. Geophys. Geosyst.* **10**, 1–13 (2009).
95. Mader, H. M., Llewellin, E. W. & Mueller, S. P. The rheology of two-phase magmas: A review and analysis. *J. Volcanol. Geotherm. Res.* **257**, 135–158 (2013).
96. Kolzenburg, S., Giordano, D., Hess, K. U. & Dingwell, D. B. Shear Rate-Dependent Disequilibrium Rheology and Dynamics of Basalt Solidification. *Geophys. Res. Lett.* **45**, 6466–6475 (2018).

Acknowledgements

F.D.F, A.P. and P.S. acknowledge the funding by MUR-PNRR Project MEET "Monitoring Earth Evolution and Tectonics" (Grant #D53C22001400005). A.V. and C.R. acknowledge the funding by MUR-PRIN Project P20222BP7J. DDG acknowledges the funding by Deutsche Forschungsgemeinschaft (DFG) project DI 2751/2–1 and the funding from the European Research Council (ERC) under the European Union's Horizon 2020 research and innovation programme (NANOVOLC, ERC Consolidator Grant–No. 101044772). J.T. and P.S. acknowledge the funding from INGV Departmental Strategic Project UNO. Special thanks go to Manuela Nazzari for assistance with microprobe analysis. This work has been greatly improved by the helpful and thoughtful reviews of Benjamin J. Andrews and one anonymous reviewer. Carolina Ortiz Guerrero is also acknowledged for the valuable editorial guidance.

Author contributions

Conceptualization: F.D.F., A.V., D.D.G. Funding acquisition: A.V., P.S. Investigation: F.D.F. Methodology: F.D.F., A.V. Resources: A.V., C.R. Supervision: A.V., D.D.G. Visualization: F.D.F., A.V., D.D.G., L.C. Writing-original draft: F.D.F. Writing-review and editing: F.D.F., A.V., D.D.G., A.P., L.C., S.M., J.T., C.R., P.S.

Competing interests
The authors declare no competing interests.

Additional information
Supplementary information The online version contains supplementary material available at https://doi.org/10.1038/s43247-024-01452-1.

Correspondence and requests for materials should be addressed to Fabrizio Di Fiore.

Peer review information Communications Earth & Environment thanks Jean Louis Vigneresse, Ben Andrews and the other, anonymous, reviewer(s) for their contribution to the peer review of this work. Primary Handling Editor: Carolina Ortiz Guerrero. A peer review file is available.